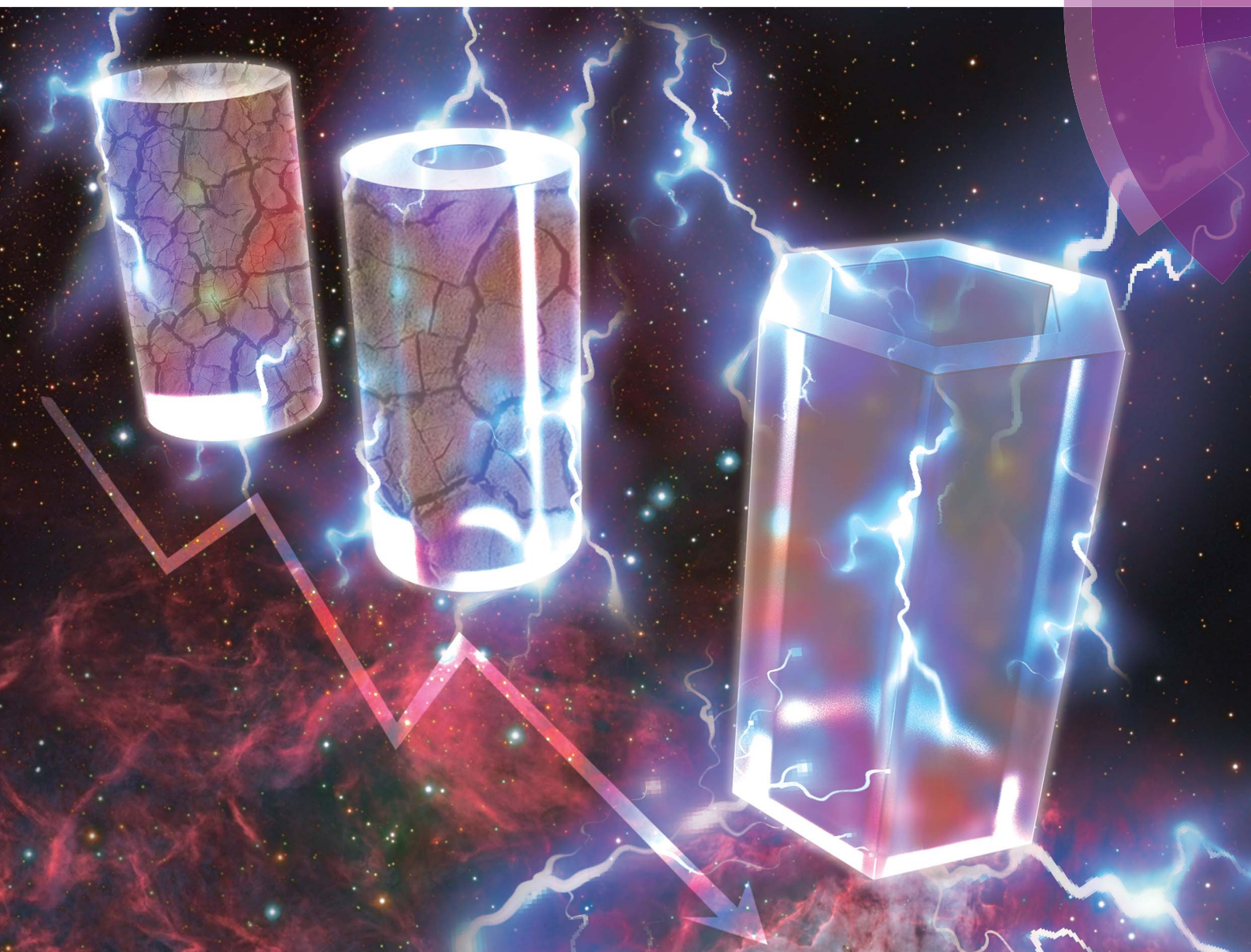


Journal of Materials Chemistry A

Materials for energy and sustainability

rsc.li/materials-a



ISSN 2050-7488



PAPER

Hao-Sen Chen, Yujie Wei, Dai-ning Fang *et al.*
Geometric design of micron-sized crystalline silicon anodes through
in situ observation of deformation and fracture behaviors

Cite this: *J. Mater. Chem. A*, 2017, 5, 12793

Geometric design of micron-sized crystalline silicon anodes through *in situ* observation of deformation and fracture behaviors†

Xing-yu Zhang,^a Wei-Li Song,^b Zhanli Liu,^c Hao-Sen Chen,^{*b} Teng Li,^d Yujie Wei^{*e} and Dai-ning Fang^{*ab}

Large anisotropic volume expansion during lithiation leads to the electrochemical performance degradation and premature fracture of micro-sized silicon electrodes in lithium-ion batteries, which prohibits its practical applications. To date, the failure mechanism of micron-size silicon electrodes has not been fully comprehended due to the lack of convincing experiments. For good understanding of lithiation/delithiation processes in the silicon anodes, in the present contribution, *in situ* observation of anisotropic volume expansion, crack initiation, penetration, deflection and delamination at the amorphous/crystalline silicon interface has been reported. The observation suggests that novel hollow and anisometric geometric electrodes have shown substantially enhanced capability in improving the fracture behaviors of the crystalline micropillar electrodes, implying that geometric design greatly impacts the strain alleviation and reversible volume change. Due to more favorable mechanical reliability, the anisometric geometric silicon electrode is expected to present essentially enhanced electrochemical performance and structural stability, which promises a novel strategy of designing Li-ion battery electrodes from a geometric perspective.

Received 22nd March 2017
Accepted 24th April 2017

DOI: 10.1039/c7ta02527k

rsc.li/materials-a

Introduction

High-capacity lithium-ion batteries (LIBs) have received much attention due to their significant commercial application in portable electronic devices and electric vehicles.^{1,2} Among many anode candidates, silicon has the highest theoretical specific capacity of 3579 mA h g⁻¹ at room temperature (Li_{3.75}Si) or 4200 mA h g⁻¹ when fully lithiated (Li_{4.4}Si).^{3,4} However, the pursuit of appropriate solutions to the critical problems induced by huge volume expansion up to ~300% due to lithium insertion is the primary challenge. Excessive volume expansion leads to unexpected irreversible mechanical

deformation and electrode fracture, which massively impacts the electrochemical performance.^{5–10}

Utilization of nanostructured silicon electrodes, such as nanowires, nanotubes, nanosized beaded strings, nanospheres and pomegranate-inspired nanostructures, was proved to be a promising solution, which can realize high capacity and long cycle life during repeated excessive deformation.^{11–15} Unfortunately, nanoscale silicon anodes are still facing great challenges, which substantially limit their commercialization in practical lithium-ion batteries, such as^{7,16} (1) their large specific surface area results in poor coulombic efficiency, especially in the first cycle,¹⁷ (2) the volume of the void portion leads to a low tap density¹⁸ and (3) existing high cost and poor scalability hazard the large-scale applications of nano-sized electrodes. Alternatively, employment of micron-sized silicon electrodes appears to be a more practical strategy for developing high-performance silicon-based LIBs.^{19–22}

In recent years, plenty of *in situ* and *ex situ* experimental techniques have been applied to study the morphological change, quantitative deformation and chemical components of silicon electrodes upon lithiation/delithiation, which promotes the comprehension of deformation and fracture mechanism in the electrochemical processes.^{3,23–34} For a good understanding of the related mechanism, however, only a few experiments and models have been established based on the deformation and fracture behaviors of micron-sized silicon electrodes.^{23,25,27,30,35} As exhibited in Fig. 1, possible lithiation/delithiation processes

^aState Key Laboratory for Turbulence and Complex Systems, College of Engineering, Peking University, Beijing, 100871, China. E-mail: fangdn@pku.edu.cn; Tel: +86-010-62753795

^bState Key Laboratory of Explosion Science and Technology, Institute of Advanced Structure Technology, Beijing Institute of Technology, Beijing 100081, China. E-mail: chenhs@bit.edu.cn; Tel: +86-010-68913302

^cApplied Mechanics Laboratory, School of Aerospace Engineering, Tsinghua University, Beijing 100084, China

^dDepartment of Mechanical Engineering, University of Maryland, College Park, Maryland 20742, USA

^eLNM, Institute of Mechanics, Chinese Academy of Sciences, Beijing 100190, China. E-mail: yujie_wei@lnm.imech.ac.cn; Tel: +86-010-82544169

† Electronic supplementary information (ESI) available: *In situ* optical observation platforms, more *ex situ* SEM images and *in situ* optical images of solid and hollow silicon micropillars, further illustration of electrodes with the anisometric geometry and FEM simulations. See DOI: 10.1039/c7ta02527k

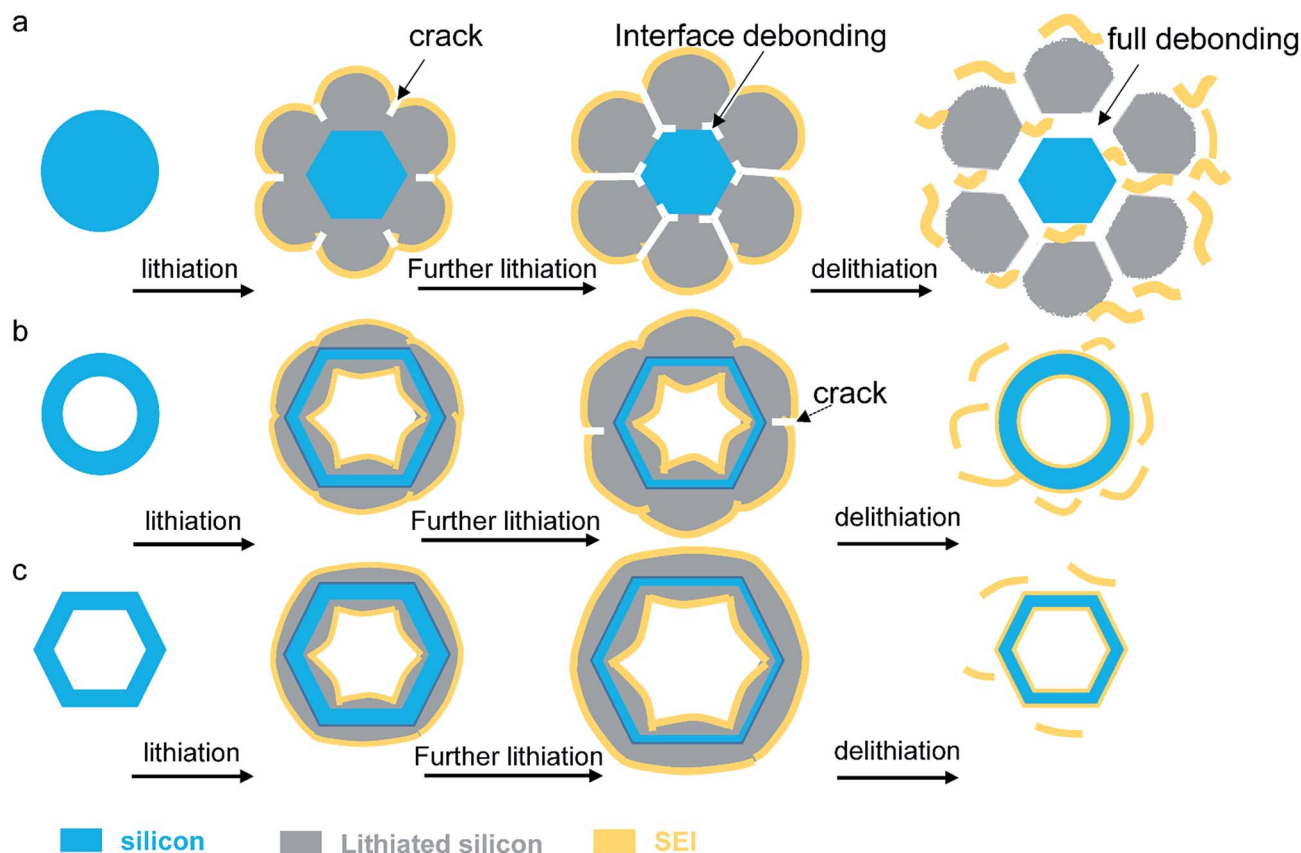


Fig. 1 Degradation mechanisms of microscale (111) c-Si electrodes as an example. (a) Crack and debonding due to anisotropic expansion of solid c-Si anodes. (b) Hollow electrode design may alleviate cracks and fractures due to the accommodation of the large volume change. (c) Anisometric geometry may avoid fracture due to circumvention of anisotropic volume change.

are illustrated for presenting the typical degradation of micron-sized c-Si electrodes, with (1 1 1) single-crystalline silicon micropillars given as an example. The anisotropic expansion of micron-sized solid electrodes leads to crack initiation and propagation, along with further debonding at the phase interface and subsequent damage in the solid electrolyte interface (SEI). Apparently, such solid electrodes present very low utilization of active materials and rapid capacity fade in the following cycles (Fig. 1a). Unfortunately, the whole failure process of micron-sized c-Si anodes has not been well proved by *in situ* experiments. More importantly, geometric design would be considered as a critical electrode factor at the micron scale since the crystalline silicon electrodes will suffer from dramatic dimensional distortion induced by 300% volume expansion.^{30,35}

In this study, *in situ* optical microscopy (*in situ* OM) was employed to investigate the entire process of anisotropic deformation and fracture behavior (crack initiation, crack propagation, crack deflection and interface delamination) for single-crystalline silicon micropillar array electrodes. For better understanding the geometric effects on the micron-sized silicon electrodes, various patterned electrode arrays (Fig. 1b and c) were explored for *in situ* investigating the evolutionary deformation and fracture behavior upon lithiation/delithiation. Both experiments and simulations collectively suggest that hollow structures (Fig. 1b and c) enable us to effectively alleviate the fracture,

compared to the solid fashion. Furthermore, anisometric hollow (Fig. 1c) electrode design indicates a favorable configuration that is more compatible with anisotropic volume expansion and could deliver enhanced electrochemical performance. Therefore, the results provide a novel route to design advanced micron-sized silicon anodes from a geometric perspective.

Experimental section

Electrode fabrication

All of the electrode arrays were directly fabricated from N-type single-crystalline Czochralski Si (111) wafers (Top Vendor Science & Technology Co. Ltd) with a resistivity of 0.002–0.004 Ω cm and a thickness of 480 ± 10 μ m. The Si micropillar diameter and space used in this work were determined according to standard photolithography, followed by a deep reactive ion etching process with the Bosch process. Equiaxial- and non-equiaxial-shaped micropillars were fabricated on the basis of the applied mask. For the purpose of enhancing an electrical contact, Ti (15 nm) and Au (100 nm) are deposited on the backside of the etching side as a current collector by a magnetron sputtering method, where Ti works as an adhesion layer to improve the adhesivity of the gold layer. Then, Cu foil, with a width of *ca.* 2 mm, was adhered to the gold layer by epoxy (Devcon) as the leading wire. All but the etching area and the

part of Cu foil as electric contact were covered in epoxy to avoid the debonding of the Au layer and control the contact zone of silicon with the electrolyte.

Electrochemical experiments

The home-made electrochemical reaction cell (Fig. S1†) is assembled in a high-purity argon filled glove box (Mbraun Inc.) with H₂O and O₂ contents <10 ppm. The components and the corresponding roles are described in detail in Fig. S1.† The electrolyte consisted of 1 M LiPF₆ in 1 : 1 (v/v) DMC : EC (Fosai New Material Co. Ltd.). All galvanostatic experiments were conducted using a multi-channel charge/discharge battery testing system (Arbin Instruments) with a lithium foil counter electrode (Alfa Aesar). Unless otherwise stated, for the lithiation (discharge), the galvanostatic current density was 450 $\mu\text{A cm}^{-2}$ above 0.1 V, and then galvanostatic discharge was adjusted to be 150 $\mu\text{A cm}^{-2}$ for 8 hours. The cycled voltage range was from 2 V to 0.05 V (vs. Li/Li⁺). After the electrochemical tests, the cell was disassembled inside the glove box and the electrodes were washed by dimethyl carbonate (DMC) for SEM imaging.

Morphological characterization

The continuous morphological changes were characterized by using an optical microscope (Keyence Corporation). The initial-state and final-state morphological changes were imaged by using a field-emission scanning electron microscope (SEM, FEI Quanta 250). The total active surface area of each sample was determined by the cross-sectional images and the top-view images before lithiation. In this process, the manufactured defects and small variations, resulting in an error in the current density calculations, were neglected. The focused ion beam machine (FEI STARTA DB235) was used to characterize the reaction depth of underneath silicon wafers that reflected the quantity of the silicon substrate that took part in the reaction.

Results and discussion

Fabrication of ordered single-crystalline silicon micropillars with different morphologies

One of the objectives in the current work is to investigate the failure process of silicon electrodes including anisotropic deformation, crack initiation, propagation and deflection, and delamination at the a-Si/c-Si interface (or electrode pulverization) using *in situ* optical characterization. To achieve this goal, deformation along the direction perpendicular to the wafer is required to be minimized for the focus stability of optical images during the experiment. According to Goldman *et al.*'s work,³⁰ the (1 1 1) single-crystalline silicon wafer was selected as a model anode to conduct the fabrication process. All the electrodes tested in this work were fabricated by the combined lithographic and dry etching protocols. In addition, the size of each micropillar should be appropriate. They are required to be appropriate to achieve good resolution by using an optical microscope and, meanwhile, to be compatible with realistic electrode scales. Silicon micropillars with a diameter of about

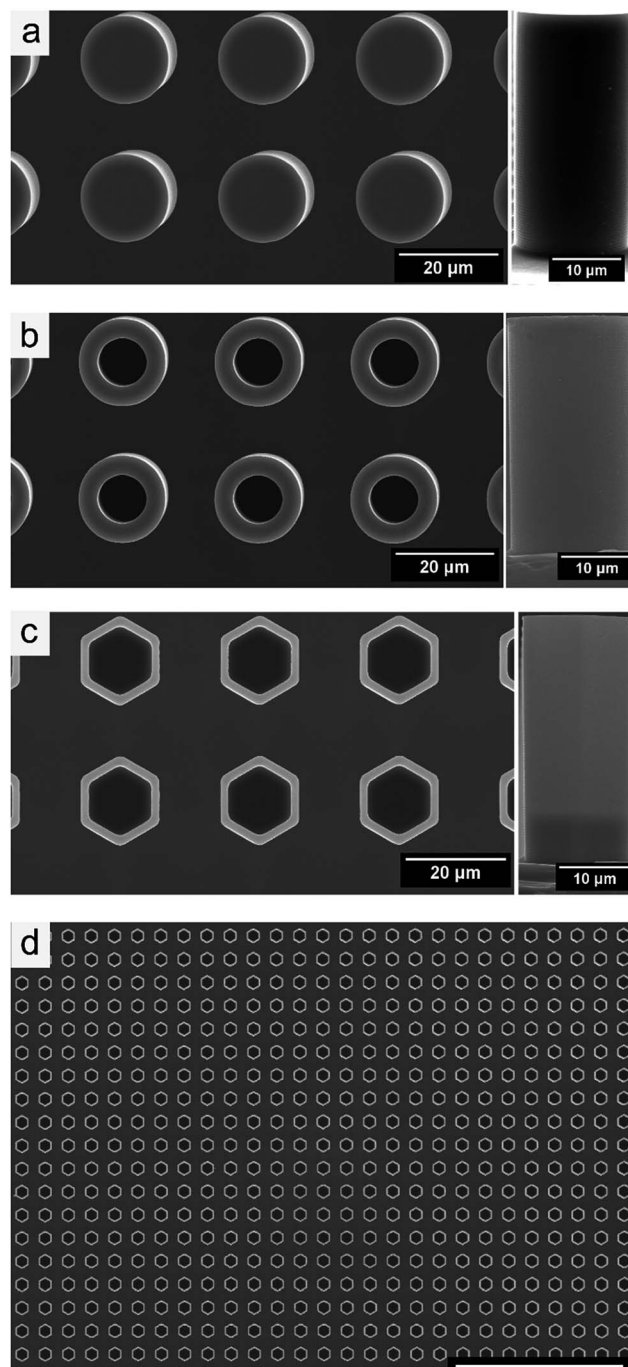


Fig. 2 Typical SEM images of (a) single-crystalline solid silicon micropillar arrays, (b) one of the isometric-hollow silicon micropillars, (c) anisometric-hollow silicon micropillars and (d) wide-range anisometric micropillars with few defects. Here, the scale bar of (d) is 200 μm .

20 μm were designed and fabricated, and a typical structure is shown in Fig. 2a.

In this work, solid microstructures of 20 μm diameter pillars with 10 μm gap (Fig. 2a) were fabricated to primarily investigate the failure mechanism of single-crystalline silicon electrodes. In addition, hollow nanoparticles, compared to solid nanoparticles, have advantages in terms of electrochemical performance due to their higher specific surface area and capability of

accommodation of volume change.³⁶ Moreover, isometric-hollow (ring-shaped) silicon micropillars (Fig. 2b) were designed to examine the deformation, fracture mechanisms and hollow structural effects on the electrochemical performance. The anisometric-hollow structures were also fabricated by combining the advantages of hollow and anisometric design.³⁵ Interior and exterior sides of the hollow hexagon prism were all $\{1\ 1\ 0\}$ crystal planes as shown in Fig. 2c. The entire fabrication process that enables a regular microstructure and feasible tailoring of structural design supplied a pathway to efficiently examine the fracture mechanism of single-crystalline silicon electrodes by an *in situ* optical method. The total etching area of each sample was $5\text{ mm} \times 5\text{ mm}$ in size with few defects (Fig. 2d).

In situ optical microscope observation

Due to the requirements of the optical method, all of the silicon arrays were fabricated on a $(1\ 1\ 1)$ single-crystalline silicon wafer. For micron-sized silicon electrodes, *in situ* OM conducted in this work is able to record and analyze the entire evolutionary process of the silicon electrodes (Fig. S1†), which is not available on the conventional *ex situ* SEM. In order to understand the kinetic fracture mechanism of $(1\ 1\ 1)$ c-Si, the optical images during the entire lithiation process were recorded every few minutes (or one minute in the important period). Prior to analysis, validation of optical images should be considered whether the selected region is representative to the whole micropillar electrode along the axial direction. According to the observation from Fig. S2,† the deformation was homogeneous and consistent with a large area of silicon electrodes, and the surface information is linked with the morphological change along the axial direction simultaneously. Note that four key evolution steps for the solid etching patterns (Fig. 3a) during lithiation at $72.9\ \mu\text{A cm}^{-2}$ are shown in Fig. 3a–d (ESI Movie S1†). The first step represented the early stage of deformation before crack initiation. As the lithiation proceeded, the crack occurred at the surface of some micropillars located at the $\{1\ 1\ 2\}$ lateral surfaces between neighboring $\{1\ 1\ 0\}$ crystal planes, when the local stress exceeded the fracture strength of lithium-silicide (assigned as the second step). Then, the crack penetrated towards the crystalline core along the $\{1\ 1\ 2\}$ lateral surface (assigned as the third step). The micro-sized silicon electrodes in the first three steps were almost consistent with the nanosized or sub-micron silicon electrodes.^{28,31} Also, Wang and co-authors briefly reported these results of the first three steps by *ex situ* SEM, but lacked continuous and direct experimental observation.²⁵ With continuous lithiation, the crack may approach the a-Si/c-Si interface and subsequently deflect along the interface. Subsequently, this lithium-silicide fraction may separate from micropillars (Fig. 3d and g). Shi *et al.* also reported the crack deflection and propagation along the a-Si/c-Si interface in the single-crystalline silicon wafers.²³ In addition, phase separation was observed by SEM in the study of micron-sized silicon bars, but it was not well illustrated in the literature.³⁰ Here, the whole process of deformation and fracture during lithiation was obtained by *in situ* OM.

To illustrate the experiment, a 2D model of a single micropillar was established and analyzed by FEM (Fig. 3h). Lithiation

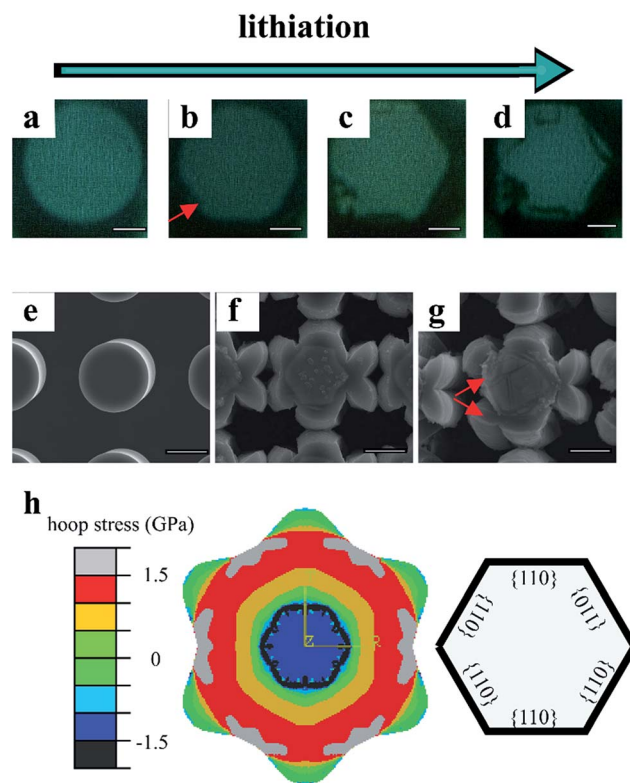


Fig. 3 Four steps characterized by using an *in situ* optical microscope during lithiation. (a) Volume expansion before crack initiation. (b) Crack initiation. Red arrow shows the location of the initial crack. (c) Crack propagation. (d) Crack deflection at the a-Si/c-Si interface and detachment of lithium-silicide from the micropillars. Here, all the scale bars are $5\ \mu\text{m}$. SEM images of the electrode sample (e) before lithiation and (f and g) after lithiation at $72.9\ \mu\text{A cm}^{-2}$. Here, the red arrow shows the crack deflection and interface delamination at the a-Si/c-Si interface. All the scale bars are $10\ \mu\text{m}$. (h) Hoop stress contour of $(1\ 1\ 1)$ Si micropillars obtained by FEM after the dimensionless time $\tau = 0.5$, defined as $\tau = TV_{\text{max}}/L$, where T is the current time, V_{max} is the maximum interface velocity, and L is the electrode feature size (e.g. pillar radius, wall thickness). The locations of stress concentration are consistent with fracture starting locations, which is in agreement with our experimental observation.

kinetics was analogous to the thermal kinetics. Based on the two-phase diffusion (Fig. 3f and g), the moving phase interface was simulated by specifying a moving temperature field. The crystalline silicon and lithium-silicide were both assumed as isotropic elastic and perfectly plastic materials, respectively, where the Cowper–Symonds overstress power law with suitable parameters was applied to approximate the perfectly plastic limit (elastic modulus $E = 185\ \text{GPa}$, Poisson's ratio $\nu = 0.28$ and yield strength $Y = 7\ \text{GPa}$ for c-Si, while $E = 35\ \text{GPa}$, $\nu = 0.22$ and $Y = 1.5\ \text{GPa}$ for a-Si). Here, the plane strain condition was used to simulate the electrode deformation due to the experimental observation of slight variation of height in the axial direction and larger size along the vertical orientation than the in-plane dimensions. The anisotropic deformation profile of a partially lithiated micropillar is shown in Fig. 3h, together with contours of hoop stress. The deformation along the $(1\ 1\ 0)$ crystalline orientation was the most prominent due to its faster lithium

invasion, and the maximum hoop stress located between neighboring $\{1\ 1\ 0\}$ planes exceeded the yield strength of a-Si. Therefore, the anisotropic expansion results in the stress concentration, thereby explaining crack initiation and the fracture starting point, in agreement with our experimental results and previous report.^{28,30} Moreover, oblique crack deflection of micropillars at the interface between a-Si/c-Si can be explained from the fracture mechanics based concept by the analysis of set B of problems in He and Hutchinson's previous work,³⁷ wherein they elaborately discussed the competition between deflection and penetration when an oblique crack impinged an linear-elastic interface between two dissimilar materials. They found that, for Dundurs' parameter $\alpha > 0.5$ ($\alpha = (\bar{E}_1 - \bar{E}_2)/(\bar{E}_1 + \bar{E}_2)$, where $\bar{E} = E/(1 - \nu^2)$), an oblique crack inside a more compliant material (corresponding to material 2, *e.g.* a-Si) was most likely to deflect along the interface due to the coincidence of the critical penetration crack with the deflecting crack, which well explained the deflection of oblique cracks in our experimental observations (because α for a-Si/c-Si is approximately equal to 0.69, and the stiffness of c-Si is much larger than that of a-Si according to above selected parameters).

Geometry design for improved fracture resistance

According to the simulated results obtained by FEM, the stress or strain concentration that originates from the anisotropic expansion was responsible for the crack initiation. Construction of hollow nanosized structures is apparently considered as the most feasible strategy to accommodate excessive volume change, which has received extensive attention in the academic world. However, few attempts have been made to validate the availability of hollow micro-sized silicon electrodes on the alleviation of strain concentration. In this work, four types of electrodes with different thickness–radius ratios ($t/R = 1, 0.70, 0.45,$ and 0.23) were fabricated by photolithography. Each type of electrode was lithiated (discharging) at $450\ \mu\text{A cm}^{-2}$ above $0.1\ \text{V}$, and then at $150\ \mu\text{A cm}^{-2}$ for 8 hours, that is, these electrodes were galvanostatically discharging at the same current density. Note that the setting current gradually reduced with the ratio increasing due to the reduction of the surface area. The morphological changes characterized by SEM and *in situ* OM are shown in Fig. 4. Anisotropic deformation and fracture behaviors (crack starting location and crack propagation) of the micropillars with (hollow) $t/R = 0.70$ and 0.45 were similar at the outside surfaces with (solid) $t/R = 1$ (Fig. 4e–g). Plots of voltage *vs.* lithiation time, and three typical steps (expansion, crack initiation, and crack propagation) of the corresponding optical images (ESI Movie S2–5†) are presented in Fig. 4i–l. Here, the voltage plateaus during lithiation were below $0.12\ \text{V}$, indicating that most of the lithium ions are inserted into the micropillars below this voltage. Additionally, no obvious deformation was observed above $0.12\ \text{V}$ (Fig. S3a and b†). Thus, the lithiation time was defined as $T = T_t - T_{U=0.12\ \text{V}}$ to eliminate the effects of the side reaction, where T_t is the total discharging time, $T_{U=0.12\ \text{V}}$ the discharging time at $U = 0.12\ \text{V}$. From Fig. 4, lithiation rates at the inner surface were slower than those at the outside surface due to the setting position of the lithium foil and

electrode (Fig. S1†). In addition, no cracks occurred at the inner surface, because they suffered from compressive stress. Instead, for the case $t/R = 0.23$, crack initiation was not observed as in the other three cases (Fig. 4d and h). However, the micropillars with $t/R = 0.23$ were also found to suffer from structural distortion upon deep lithiation, which may be induced by the combined effects of asymmetric lithium flux and thin-wall feature. This result indicated that a hollow structure with $t/R = 0.23$ can avoid fracture at appropriate lithiation depth, and enhance the utilization of active materials.

When galvanostatically discharging at the same current density, fracture occurred in the silicon micropillars with the thickness–radius ratios $t/R = 1, 0.70$ and 0.45 . The analysis and statistics of fracture behavior are shown in Fig. 5 (the case $t/R = 0.23$ was not discussed here due to no obvious fracture). The lithiation time of initial fracture and the corresponding relative depth of lithiation increased with the decreased thickness–radius ratio (Fig. 5a). The former was obtained through the analysis of optical images and discharging data, while the latter was based on discharging data collected by using a charging–discharging electrochemical system (details discussed in the caption of Fig. S3†). Thus, isometric-hollow structures can delay the initial fracture and enhance the utilization of active materials. In addition, with the above mentioned FEM, these three types of configurations were simulated (more details in ESI Note S1†). The setting parameters and assumptions are identical to those in the previous section. Based on the experimental observation that the lithiation rate at the inner surface was slower than that at the outside surface, the rate of the moving temperature field at the outside surface is larger than that at the inner surface. Through the FEM simulation, the anisotropic deformation is in good agreement with the experimental observation. From the equivalent plastic strain (PEEQ) contour, the location of the PEEQ concentration is consistent with the initial crack location (Fig. 5c and d). Fig. 5b shows the PEEQ distribution along the $\{1\ 1\ 2\}$ crystal orientation between the neighboring $\{1\ 1\ 0\}$ surfaces. The maximum of PEEQ decreases as the thickness–radius ratio reduces, which accordingly diminishes the fracture risk, in agreement with the consequences obtained from Fig. 5a. Despite the presence of fracture behavior for the single-crystalline silicon micropillars with a relatively large thickness–radius ratio (*e.g.* $t/R > 0.45$), crack initiation can be delayed, and hollow structures can also increase active material utilization. Moreover, thin-wall micro-electrodes may avoid fracture during the first deep lithiation (*e.g.* $t/R = 0.23$ in this work).

One of the design rules for ring-shaped single-crystalline silicon micropillars aims at enhancing the capability of alleviating fracture (CAF) in order to realize combined functions of mechanical integrity and high material utilization. Based on the experimental observation, FEM simulation and theoretical analysis, the relationship between CAF and design parameter t/R is summarized in Fig. 6. According to the experimental observation after first lithiation, a smaller thickness–radius ratio had an advantage of higher capability to alleviate the fracture because of a slower approach to the critical PEEQ (Fig. 6a). The critical PEEQ is hypothetical (because of no

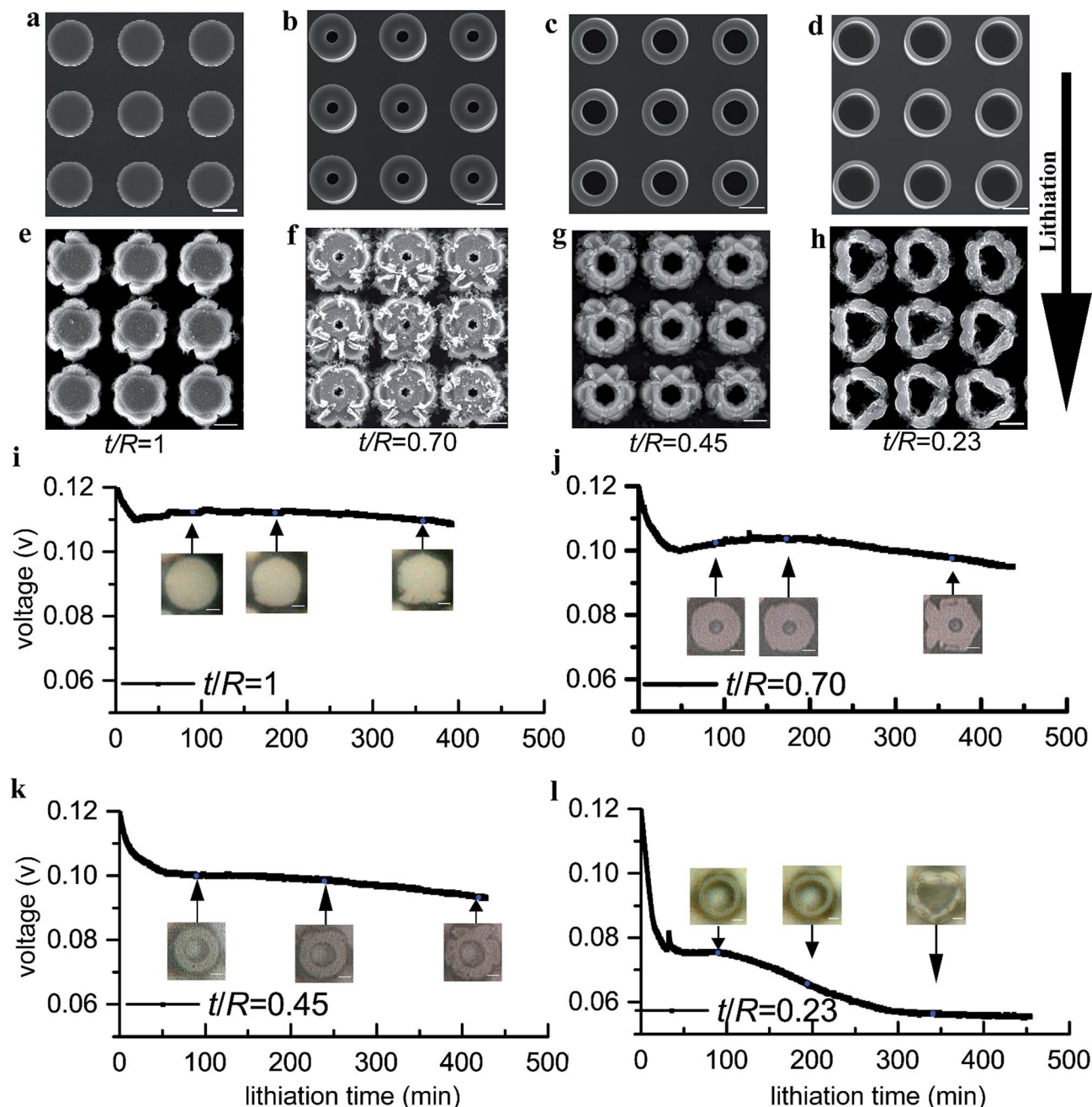


Fig. 4 Top-view SEM images of single-crystalline (1 1 1) silicon electrodes with different thickness–radius ratios before lithiation (a–d) and after lithiation (e–h). Galvanostatic discharge (lithiation) current density is $450 \mu\text{A cm}^{-2}$ above 0.1 V, and then galvanostatic discharge is set to be $150 \mu\text{A cm}^{-2}$ for 8 hours. The scale bars are 10 μm . Plots of voltage vs. lithiation time for silicon electrodes with (i) $t/R = 1$, (g) $t/R = 0.70$, (j) $t/R = 0.45$, (l) $t/R = 0.23$ reflecting three typical lithiation stages. The first stage is the expansion process before crack initiation; the second stage reflects the crack initiation process due to the excess lithium insertion; the third stage represents the crack propagation process. The scale bars in inserted optical graphs are 5 μm .

experimental data) and relatively conservative (due to crack initiation below this critical PEEQ). The CAF is benchmarked against the normalized lithiation time of initial fracture, defined as $\tau^* = T_i/T_{t/R=1}$, below which no cracks are generated. T_i is the lithiation time of initial fracture of electrodes with different t/R , while $T_{t/R=1}$ is the lithiation time of initial fracture of electrodes with $t/R = 1$. The time when the PEEQ value approaches the hypothetical critical PEEQ is defined as the

lithiation time of initial fracture in the simulation. Surprisingly, the tendency of CAF based on the conservative critical PEEQ is in good agreement with experimental results under the experimental limitation in this work, which provides a design rule to enhance the fracture resistance of single-crystalline silicon micropillars. Here, there is no or slighter enhancement of CAF when the inner radius is small (*i.e.* t/R approaches to 1), which can be explained by the stress analysis for thick-wall electrodes.

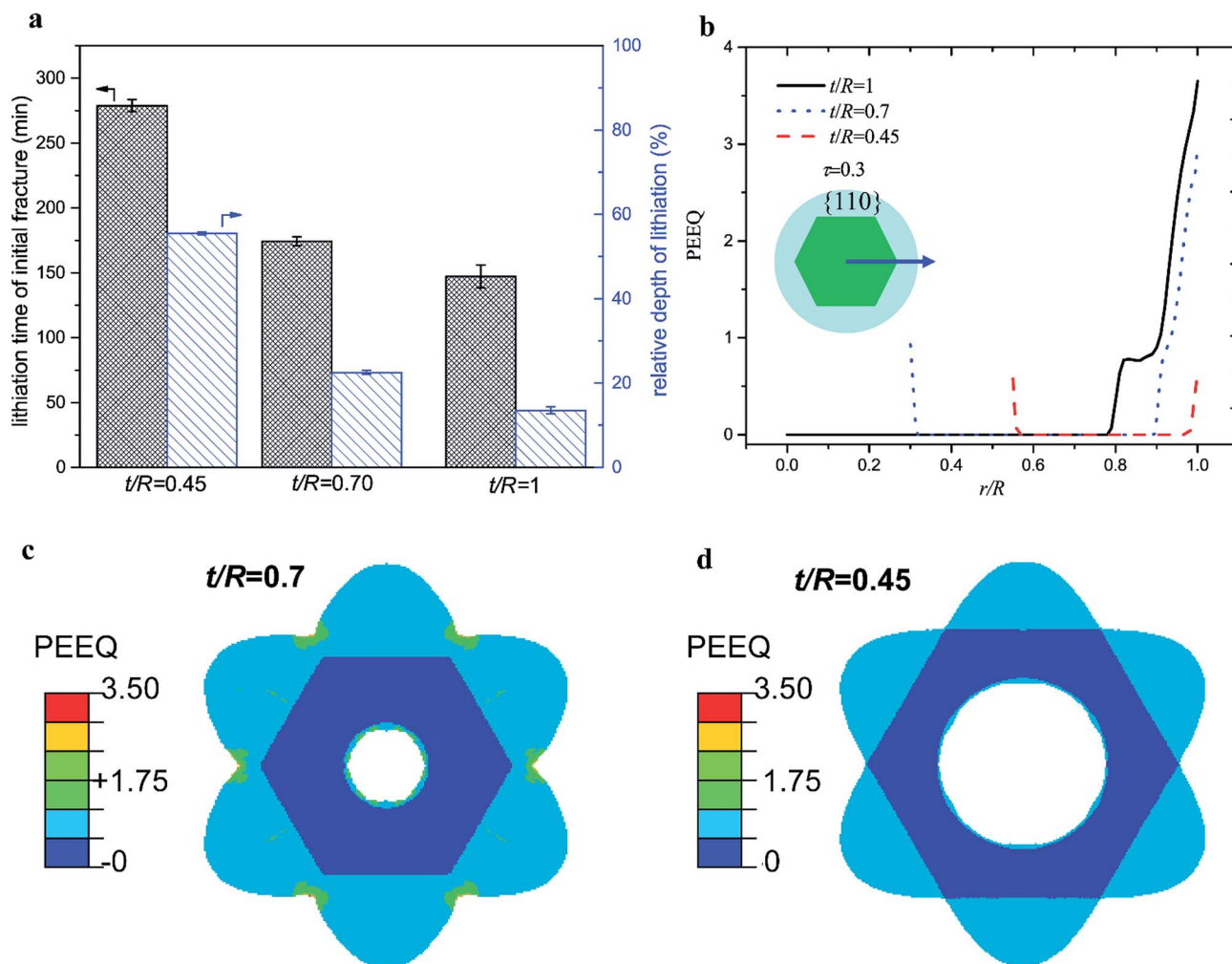


Fig. 5 (a) Column chart of the lithiation time of initial fracture and the relative depth of lithiation. The galvanostatic current density is consistent with that in Fig. 4. (b) PEEQ values at different location r/R along the radial direction (*i.e.* along the direction of the blue arrow in the inserted graph) for different ratios of t/R obtained by finite element analyses; the dimensionless time is $\tau = 0.3$. The corresponding PEEQ cloud images of finite element analyses with (c) $t/R = 0.70$ and (d) $t/R = 0.45$ at $\tau = 0.3$.

The hoop stress for thick-wall electrodes and solid ones in the a-Si can be given in the same formula,³⁸

$$\sigma_{\theta} = \frac{2}{\sqrt{3}} Y \log(r/r_0) + \frac{2}{\sqrt{3}} Y \quad (A < r < r_0) \quad (1)$$

where r_0 is the current outside radius, and A is the location of the a-Si/c-Si interface. Thus, the CRF in this case has no difference during lithiation at the same current density. The CAF of moderate thick-walls (*e.g.* $t/R = 0.70$ and $t/R = 0.45$) has a greater improvement due to larger space to accommodate the volume change. For thin-wall electrodes with t/R below a threshold value (*e.g.* $t/R = 0.23$), CAF is distinctly enhanced to avoid fracture during the first lithiation (even nearly full lithiation). Note that the structural distortion may occur under over-discharge (over-lithiation) for the thin-wall electrodes. Consequently, alleviation of fracture can be achieved in the micron-sized single-crystalline silicon electrodes, under the rules of structure designs or controlling the lithiation depth.

Anisometric geometry for enhanced electrochemical performance

The strain or stress concentration during lithium insertion into the silicon electrodes is attributed to the anisotropic deformation along the different crystalline orientations (*e.g.* six locations at the outside surface between neighboring two $\{1\ 1\ 0\}$ crystal planes for $(1\ 1\ 1)$ c-Si in Fig. S4a†), which inspires a novel design strategy that gives the slow moving orientation larger dimensions, and thus the anisotropy seems to be more uniform in volume changes for alleviating the strain concentration. In the previous work by An *et al.*, anisometric morphologies of the solid c-Si structures were designed and simulated by FEM to manifest the mitigation of lithiation-induced fracture.³⁵ However, the serious fracture issue still occurred in the anisometric solid c-Si electrodes. Therefore, anisometric-hollow single-crystalline silicon arrays with hexagonal prism microstructures were designed and fabricated in this work (Fig. 2c and S4b†). Interestingly, the anisometric hollow c-Si configuration exhibited to

counteract the anisotropy during partial lithiation (Fig. 7a and b). The kinetic deformation behaviour of the anisometric-hollow electrodes was also investigated by *in situ* OM under the same electrochemical conditions, which showed no obvious fracture except for larger structural distortion. This result indicates that c-Si electrodes with anisometric structures are helpful to alleviate fracture and reduce the capacity loss due to the mechanical stability. In order to compare the electrochemical properties

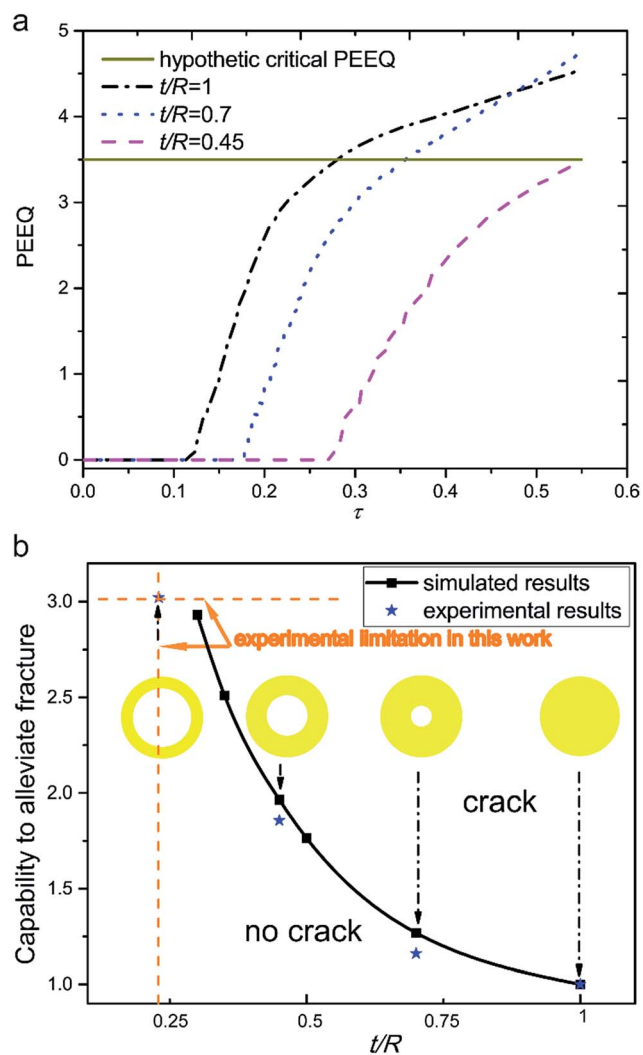


Fig. 6 (a) Plots of PEEQ vs. lithiation dimensionless time τ obtained by the FEM simulation. Here, the PEEQ of a smaller thickness–radius ratio t/R is more delayed in reaching the hypothetical critical PEEQ below which no cracks occur. (b) Capability to alleviate fracture (CAF) vs. thickness–radius t/R during first lithiation for single-crystalline silicon micropillars based on experimental observations (Fig. 5), simulated results (a). Here, CAF is defined as the normalized lithiation time of initial fracture ($\tau^* = T_i/T_{i/R=1}$) below which no cracks can be generated. T_i is the lithiation time of initial fracture of electrodes with different t/R values, while $T_{i/R=1}$ is the lithiation time of initial fracture of electrodes with $t/R = 1$. The lithiation time of initial fracture in simulated results is when the PEEQ value is up to the hypothetical critical PEEQ (a). The tendency of CAF according to the conservative critical PEEQ is in good agreement with experimental results under experimental limitations in this work. Here, the magenta line is an inferred line based on the experimental observation of electrodes with $t/R = 0.23$.

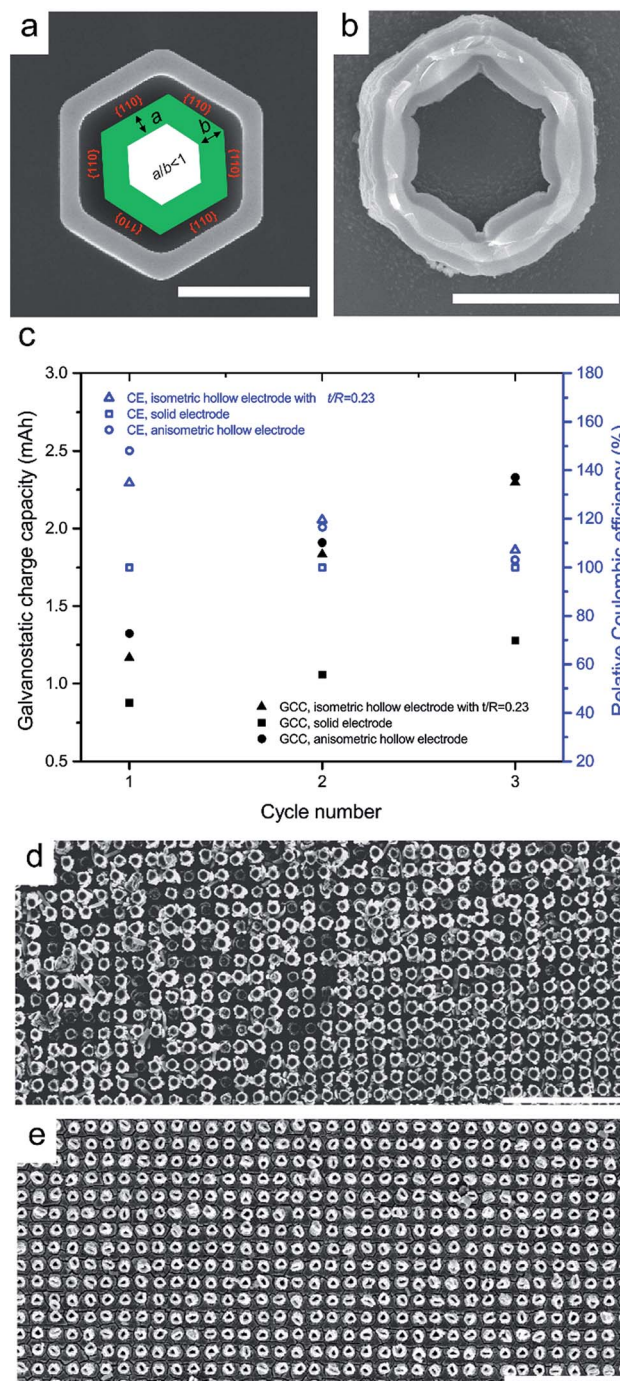


Fig. 7 SEM images of single-crystalline silicon micropillars with hexagonal prism structures (a) before lithiation and (b) after lithiation at $150 \mu\text{A cm}^{-2}$ for 5 hours. The anisometric parameter is defined as $\lambda = a/b$ (inserted graph in figure). The parameter λ changes to 1.17–1.33 from $\lambda = 0.66$ after lithiation, which confirmed that anisometric structures circumvented the anisotropy. Here, the scale bars are 10 μm (a and b). (c) Charge (delithiation) capacity (GCC) and relative coulombic efficiency (CE) of anisometric electrodes and isometric electrodes with $t/R = 0.23$ galvanostatic discharge/charge cycled at the same current density demonstrated better electrochemical properties than solid structures. The relative CE is defined as the computed CE divided by CE of solid electrodes at each cycle (*i.e.* CE of solid electrodes is deemed to be a basis). Top-view SEM images of (d) solid electrodes and (e) anisometric hollow electrodes after the three cycles. Here, the scale bars are 200 μm (d and e).

(solid electrodes, isometric-hollow ones with $t/R = 0.23$ and anisometric hollow ones), galvanostatic charge (delithiation) capacity and coulombic efficiency of these electrodes are plotted in Fig. 7c for the first three cycles. The anisometric hollow single-crystalline silicon electrodes had the largest galvanostatic charge capacity and highest coulombic efficiency at the first charge/discharge cycle, which is attributed to the alleviation of the strain concentration and maintenance of the mechanical integrity (ESI Movie S8†). The isometric hollow electrodes with $t/R = 0.23$ had greater electrochemical properties than solid electrodes, which was consistent with the analysis of fracture behavior in the previous section. It is noticeable that anisometric and isometric electrodes suffered from extreme over-discharge (lithiation) conditions, especially after the first cycle, because the silicon substrate (the part under the etching micropillars) was accompanied by serious lithiation and delithiation (Fig. S5†). However, under severe electrochemical conditions, the anisometric and isometric hollow c-Si electrodes still showed much enhanced coulombic efficiency. Therefore, the strategy of migrating the fracture behavior by geometric design is valid for micron-sized single-crystalline silicon electrodes. Additionally, the morphological changes after three charging/discharging cycles were probed by SEM (Fig. 7d and e). A larger fraction of solid c-Si micropillars were delaminated from the substrate, while abundant lithium-silicide phases were detached from the micropillars (ESI Movie S6†), which leads to lower capacity retention, inefficient utilization of active materials and poor coulombic efficiency. In the contrary, the isometric electrode with $t/R = 0.23$ and the anisometric electrode had very few micropillars delaminated from the substrate. The volume shrinkage of these two structures during delithiation was observed in ESI Movies S7 and S8†. Therefore, higher coulombic efficiency was attributed to the less irreversible capacity loss and higher mechanical integrity. Consequently, geometric design that enables to alleviate the strain concentration due to anisotropic deformation provides a new strategy to fabricate more durable single-crystalline silicon electrodes.

Conclusion

In summary, the fracture behavior of a single-crystalline silicon electrode with micropillar arrays was investigated by using an *in situ* optical microscope. The whole processes of anisotropic volume expansion, crack initiation, crack penetration, crack deflection and delamination at the a-Si/c-Si interface are observed. With analysis by experiment and simulation, the results suggest that the anisometric design has a significant impact on the mechanical integration and electrochemical performance of the silicon electrode arrays, which highlights a novel platform for rationally designing high-performance micron-size silicon anodes for LIBs.

Acknowledgements

The authors are grateful for the support by the National Natural Science Foundation of China under grants #11672341, #111572002. Support by the Foundation for Innovative Research

Groups of the National Natural Science Foundation of China is also acknowledged (Grant No. 11521202). The work is also financially supported by the National Materials Genome Project (2016YFB0700600).

Notes and references

- 1 B. Dunn, H. Kamath and J. M. Tarascon, *Science*, 2011, **334**, 928–935.
- 2 R. Van Noorden, *Nature*, 2014, **507**, 26–28.
- 3 J. Li and J. R. Dahn, *J. Electrochem. Soc.*, 2007, **154**, A156–A161.
- 4 M. T. McDowell, S. W. Lee, W. D. Nix and Y. Cui, *Adv. Mater.*, 2013, **25**, 4966–4985.
- 5 U. Kasavajjula, C. Wang and A. J. Appleby, *J. Power Sources*, 2007, **163**, 1003–1039.
- 6 Y. F. Gao, M. Cho and M. Zhou, *Journal of Mechanical Science and Technology*, 2013, **27**, 1205–1224.
- 7 B. Liang, Y. Liu and Y. Xu, *J. Power Sources*, 2014, **267**, 469–490.
- 8 M. T. McDowell, S. Xia and T. Zhu, *Extreme Mechanics Letters*, 2016, **9**, 480–494.
- 9 S. Zhang, *npj Computational Materials*, 2017, **7**, 1–11.
- 10 Y. Lia, J. Yang and J. Song, *Renewable Sustainable Energy Rev.*, 2017, **74**, 19–25.
- 11 H. Wu, G. Chan, J. W. Choi, I. Ryu, Y. Yao, M. T. McDowell, S. W. Lee, A. Jackson, Y. Yang, L. Hu and Y. Cui, *Nat. Nanotechnol.*, 2012, **7**, 310–315.
- 12 Y. Yao, M. T. McDowell, I. Ryu, H. Wu, N. Liu, L. Hu, W. D. Nix and Y. Cui, *Nano Lett.*, 2011, **11**, 2949–2954.
- 13 N. Liu, Z. Lu, J. Zhao, M. T. McDowell, H. Lee, W. Zhao and Y. Cui, *Nat. Nanotechnol.*, 2014, **9**, 187–192.
- 14 C. Sun, K. Karki, Z. Jia, H. Liao, Y. Zhang, T. Li, Y. Qi, J. Cumings, G. W. Rubloff and Y. Wang, *ACS Nano*, 2013, **7**, 2717–2724.
- 15 C. K. Chan, H. Peng, G. Liu, K. McIlwrath, X. F. Zhang, R. A. Huggins and Y. Cui, *Nat. Nanotechnol.*, 2008, **3**, 31–35.
- 16 Y. Sun, N. Liu and Y. Cui, *Nat. Energy*, 2016, **1**, 16071.
- 17 Y. Zhao, X. Liu, H. Li, T. Zhai and H. Zhou, *Chem. Commun.*, 2012, **48**, 5079.
- 18 I. H. Son, J. Hwan Park, S. Kwon, S. Park, M. H. Rummeli, A. Bachmatiuk, H. J. Song, J. Ku, J. W. Choi, J. Choi, S. Doo and H. Chang, *Nat. Commun.*, 2015, **6**, 7393.
- 19 Z. Chen, C. Wang, J. Lopez, Z. Lu, Y. Cui and Z. Bao, *Adv. Energy Mater.*, 2015, **5**, 1401826.
- 20 Z. Lu, N. Liu, H. Lee, J. Zhao, W. Li, Y. Li and Y. Cui, *ACS Nano*, 2015, **9**, 2540–2547.
- 21 L. A. Berla, S. W. Lee, I. Ryu, Y. Cui and W. D. Nix, *J. Power Sources*, 2014, **258**, 253–259.
- 22 C. Wang, H. Wu, Z. Chen, M. T. McDowell, Y. Cui and Z. Bao, *Nat. Chem.*, 2013, **5**, 1042–1048.
- 23 F. Shi, Z. Song, P. N. Ross, G. A. Somorjai, R. O. Ritchie and K. Komvopoulos, *Nat. Commun.*, 2016, **7**, 11886.
- 24 S. W. Lee, H. Lee, I. Ryu, W. D. Nix, H. Gao and Y. Cui, *Nat. Commun.*, 2015, **6**, 7533.
- 25 J. C. Ye, Y. H. An, T. W. Heo, M. M. Biener, R. J. Nikolic, M. Tang, H. Jiang and Y. M. Wang, *J. Power Sources*, 2014, **248**, 447–456.

- 26 M. Pharr, K. Zhao, X. Wang, Z. Suo and J. J. Vlassak, *Nano Lett.*, 2012, **12**, 5039–5047.
- 27 Y. He, X. Yu, G. Li, R. Wang, H. Li, Y. Wang, H. Gao and X. Huang, *J. Power Sources*, 2012, **216**, 131–138.
- 28 S. W. Lee, M. T. McDowell, L. A. Berla, W. D. Nix and Y. Cui, *Proc. Natl. Acad. Sci. U. S. A.*, 2012, **109**, 4080–4085.
- 29 I. Ryu, J. W. Choi, Y. Cui and W. D. Nix, *J. Mech. Phys. Solids*, 2011, **59**, 1717–1730.
- 30 J. L. Goldman, B. R. Long, A. A. Gewirth and R. G. Nuzzo, *Adv. Funct. Mater.*, 2011, **21**, 2412–2422.
- 31 S. W. Lee, M. T. McDowell, J. W. Choi and Y. Cui, *Nano Lett.*, 2011, **11**, 3034–3039.
- 32 F. Sun, H. Markötter, K. Dong, I. Manke, A. Hilger, N. Kardjilov and J. Banhart, *J. Power Sources*, 2016, **321**, 174–184.
- 33 A. Timmons and J. R. Dahn, *J. Electrochem. Soc.*, 2007, **154**, A444.
- 34 A. Timmons and J. R. Dahn, *J. Electrochem. Soc.*, 2006, **153**, A1206.
- 35 Y. An, B. C. Wood, J. Ye, Y. Chiang, Y. M. Wang, M. Tang and H. Jiang, *Phys. Chem. Chem. Phys.*, 2015, **17**, 17718–17728.
- 36 J. Liu and D. Xue, *Nanoscale Res. Lett.*, 2010, **5**, 1525–1534.
- 37 M. Y. He and J. W. Hutchinson, *Int. J. Solids Struct.*, 1989, **25**, 1053–1067.
- 38 Z. Jia and T. Li, *J. Power Sources*, 2015, **275**, 866–876.